Investigation on the Stabilization Behaviour of $MgAl_2O_4$ (spinel) Particles in Aluminium Foam via In-situ X-ray radioscopy and FIB tomography

G. S. Vinod Kumar[1#], K. Heim[2,3], M. Mukherjee[4,5], F. Garcia-Moreno[2,3], J. Banhart[2,3]

1. SRM University – AP, Amaravati, Andhra Pradesh, 522502, India

2. Technische Universität Berlin, Hardenbergstraße. 36, 10623 Berlin, Germany

3. Helmholtz-Zentrum Berlin für Materialien und Energie, Hahn-Meitner-Platz 1, 14109 Berlin, Germany

4. *Metal Foams and Porous Materials Lab, Department of Metallurgical and Materials Engineering, Indian Institute of Technology Madras, Chennai 600036, India*

5. Applied Magnesium Research Group - Centre of Excellence in Materials and Manufacturing for Futuristic Mobility, Indian Institute of Technology Madras, Chennai 600036, India

Corresponding Author: vinodnarasimha@gmail.com

Abstract

The paper investigates the stabilization behaviour of in-situ created, sub-micron sized $MgAl_2O_4$ (spinel) particles at various concentration in Al-11wt.%Si foams. The foam evolution (expansion, coalescence and drainage) as a function of particle concentration and foaming time was monitored in-situ using X-ray radioscopy. The foam containing higher concentration (3.4 vol.%) of $MgAl_2O_4$ exhibited higher stability and expansion until solidification. Decreasing the $MgAl_2O_4$ concentration to 2.5 vol.% exhibited similar foam expansion like 3.4 vol.% particle-containing foam, however the stability of the former is poor due to higher drainage. The foam containing lower $MgAl_2O_4$ concentration (1.7 vol.%) showed poor stability and expansion due to further increase in drainage. The 3D visualisation of $MgAl_2O_4$ particles

in the gas solid interface embedded in the oxide skin was brought out by FIB tomography. TEM analysis revealed that the nano-sized $MgAl_2O_4$ particles are closely embedded in the oxide skin.

Keywords: Closed-cell aluminium foams, Stabilization, Ceramic particles, In-situ X-ray radioscopy, FIB tomography

1. Introduction

Producing closed-cell aluminium foams through liquid metal processing requires the usage of fine ceramic particle dispersed in the aluminium melt to be foamed to ensure stability of the ensemble of metallic foams and bubbles before solidification. The stability of liquid foam depends on various forces acting directly on it such as gravity, mechanical forces, and capillary forces, etc. or indirectly, caused by surface tension, atmospheric pressure or internal gas pressure. An imbalance of these forces causes drainage, cell coalescence, film rupture, or other unwanted degradation in the liquid foam [1]. Solid particles are essential to counteract the imbalances created by various forces and to stabilize the liquid foam [1]. Such particles act as a stabilizing agent based on its concentration, morphology and wetting characteristics with the melt [2-5]. In aluminium foam, the stabilizing agents can be various things - from oxide bi-films that are inherently formed in a melt [6-8], ceramic particles that are added into the melt such as SiC [2,6,9,10] or Al_2O_3 [6,9] or particles that are created in situ in the melt such as TiC, TiB_2, ZrB_2, AlN, $MgAl_2O_4$, etc. [11-14].

A particle attaches to the gas-solid interface of foam if it is partially wetted by the liquid and then contributes to foam stabilization [1]. Note that the gas-solid interface observed in a solid foam is actually the gas-liquid interface before the foam solidifies. Sun and Gao experimentally

determined the optimum wetting angle for aqueous foam stabilization and found values from 75° to 85°. They also found that above 90° wetting angle the particles are strongly attached to the gas-solid interface of the foam. [15] This contradicts the models by Kaptay [16] who predicted that no foam stability is possible outside a range of the wetting angle from 20° to 90°. Körner et al. have proposed stabilization based on the disjoining pressure between the two gas-solid interfaces of a film caused by particles [4]. Some possible particle arrangements in a film were proposed based on the particle density measured in a foam film and based on the necessity for a mechanical disjoining force between the opposite layers (gas-liquid interfaces) of a film [1, 5, 17].

Particle size also plays a significant role in foam stabilization. Finer particles (size down to sub-micrometer) have a larger surface area per unit volume than coarser ones resulting in higher surface coverage of the gas-solid interfaces, which then enhances foam stability [2,18]. Finer particles are also numerous, which can increase the effective viscosity of the melt [2,9, 19]. Studies of individual metallic films showed that the presence of oxygen is also important for stabilization even though particles are present. Heim et al. have systematically studied the synergistic effect of particles and oxides on stabilization. [20,21]. In aluminium foam, sub-µm sized $MgAl_2O_4$ (spinel) particles have been found to be an efficient stabilizing agent [14,8,22-24]. Heim et al. demonstrated that $MgAl_2O_4$ particle-reinforced Al-9wt.%Si-0.6wt.% Mg alloy can be foamed by injecting gas [25]. $MgAl_2O_4$ particles were found embedded in the gas-solid interface of the cell walls of aluminium foam [14].

The present work focusses on the stabilization characteristics of $MgAl_2O_4$ particles in Al-11wt.%Si alloy foam as a function of the volume fraction of particles. The evolution of the liquid foam until solidification was observed in situ by X-ray radioscopy to understand the

effect of particle vol.% on stability. An in-depth microstructural analysis of the particle arrangement in the gas-solid interface of the cell wall was performed using focused ion beam tomography and TEM.

1. Experimental Procedure

Al-11wt.%Si alloy reinforced with sub-µm sized $MgAl_2O_4$ particles (spinel) was synthesized via in-situ reaction. First, ingots of Al-20wt.%Si alloy were melted together with commercial pure Al (99.7 wt.%), total quantity about 500 g, in a clay graphite crucible at 750 °C using a vertical stir casting furnace at ambient atmosphere to obtain Al-9 wt.%Si alloy. Once the melt reached the desired temperature, 5 wt.% of Mg (99.9 wt.% pure) was plunged into the melt. The melt was mechanically stirred at 600 rpm and micro-silica powder of 44 µm average particle size added at the rate of 0.5 wt.% per minute into the melt through the vortex created. After the SiO_2 particles had been completely admixed, the melt was held for 10 h at 750 °C to facilitate the reaction among SiO_2, Al and Mg. After 10 h of reaction holding the melt was cast into a cylindrical steel mould of 50 mm diameter and 200 mm height. The castings obtained were sliced and characterized by XRD using Cu Kα radiation (Bruker-AXS-D8). The phases were analysed using ICDD-PD database. The samples were metallographically ground and electro-polished for microstructural analysis using SEM (Gemini Leo 1530, Zeiss Oberkochen, Germany, equipped with EDX, Thermo-Fisher). The details of the synthesis and the elemental concentrations are given in Table 1. The composite synthesized has 3.4 vol.% of $MgAl_2O_4$ as per the calculation given in Ref. [14]. The resultant composite also contains some fine MgO particles, the content of which is difficult to calculate or measure. The 5 wt.% SiO_2 upon complete reaction with Mg and Al releases approximately 2wt.% of Si [14], which increases the Si concentration from 9 wt.% to 11 wt.%.

Table1. The in-situ composite synthesized

Elements added (Nominal composition, in wt%)				**Reaction temperature (˚C)**	**Reaction time (h)**
Mg	Si	SiO_2	Al (bal.)		
5	9	5	84	750	10

For the foaming studies, the in-situ composite with 3.4 vol% of $MgAl_2O_4$ was diluted with Al-11 wt.%Si alloy to lower the $MgAl_2O_4$ to 2.5 and 1.7 vol.% in order to study different particle volume fractions and their influence on foam stability. Foaming was carried out by an interrupted foaming method which is analogous to what is referred to as 'FORMGRIP' method [26]. It consists of two stages of foam preparation. In the first one, 100 g of composite was melted in an alumina crucible inside a furnace at 700 ˚C. After the melt had reached the desired temperature, 1.5 wt.% of pre-treated TiH_2 powder (pre-oxidised in air for 24 h at 400 °C followed by 1 h at 500 °C) was gradually admixed in 80 s using a graphite stirrer rotating at 1200 rpm. Immediately after mixing, the melt was rapidly quenched by pouring it into a water-cooled copper mould of 25 mm diameter and 100 mm height to obtain cylindrical castings. Subsequently these castings were sliced in the transverse direction to obtain the desired quantity of foamable precursor. The foamable precursors were prepared metallographically and subjected to microstructural analysis using optical microscope (Carl Zeiss) and SEM (Gemini Leo 1530, Zeiss Oberkochen, Germany equipped with EDX, Thermo Fisher). Due to the short solidification time, these precursors contained only little porosity (Ref Table 2).

Foaming experiments were performed under ambient pressure by re-melting the foamable precursor using a resistive heating plate at 750 °C and holding there for 600 s. The foaming temperature was reached within 60 s (average heating rates was ~12 K/s). For each of the three different $MgAl_2O_4$ contents, samples of identical weight (4.5 g) were foamed. After this, the heater was turned off and natural cooling took place. The sample temperature was measured

by a thermocouple fed through a hole in the bottom of the heating plate. Foam evolution was monitored by an X-ray radioscopy set-up comprising a micro-focus X-ray source with a tungsten target and a panel detector as described in Ref. [27]. In this work, the X-ray spot size was set to 5 μm while applying 100 kV voltage and 100 μA current. A series of X-ray projection images of the foaming samples were obtained with a time resolution of 2 s and analysed quantitatively using an in-house-developed image analysis software, AXIM [28]. Expansion was measured in terms of the growth of the projected area of the sample.

Table 2 – List of foaming experiments performed under in-situ X-ray radioscopy. The foaming temperature was 750 °C and the time of foaming was 600 s.

Foam code	**Precursors, absolute density (ρ) g/cm^3**	**Average Porosity, %**	**$MgAl_2O_4$ Vol.%**
3.4p	2.02	24	3.4
2.5p	2.29	14	2.5
1.7p	2.4	10	1.7

The X-ray projection images were also used for drainage analysis by employing AXIM software. For this, a 100-pixel wide area around the central vertical axis of the sample was chosen along the height of the sample. For every pixel along the height of the sample, AXIM calculates a grayscale value by averaging the grayscale values of all the 100 pixels along the width of the chosen area. Applying the Beer´s law each average grayscale value corresponds to a certain 'density' (when the sample is solid) or 'liquid fraction' (when the sample is molten). The analysis is performed for the entire foaming sequence. The highest 'density' in the entire foaming sequence is taken as 100%, which corresponds to the un-foamed precursor without considering its starting porosity mentioned in table 2.

X-ray tomography of foams was performed by rotating them through 360° in steps of 1° while acquiring X-ray radiographic images after each step. Three-dimensional (3D) reconstruction

of the data was carried out using the commercial software 'Octopus'. After reconstruction, the commercial software 'VG StudioMax 1.2.1' was used to extract 3D sections of the foam.

The shape, size and distribution of spinel particles in the 3.4p foam was analysed in detail by (i) SEM/EDX, (ii) focused-ion-beam (FIB) tomography and (iii) TEM/EDX. For (i) and (ii), a Zeiss Cross Beam 1530 EsB© workstation comprising an ultra-high-resolution GEMINI© field emission column and a gallium cannon were used. Using SEM the particles present at the inner bubble surface ie., the gas-solid interface as well as the cross section of a foam cell wall were imaged in bright field using a SE2 detector.

FIB slicing allows one to compile a tomography of the gas-solid interface of a foam cell wall for a 3D-view of the distribution and shape of $MgAl_2O_4$ particles. The slicing was carried out for an area about 15 µm × 15 µm × 15 µm at the gas solid interface. Prior to that, the top surface was protected by depositing 1 µm-thick platinum strip at 30 keV / 500 pA Ga ion beam energy/current in order to avoid ion beam induced damage and unwanted milling during sample preparation. Coarse milling was carried out to extract the volume using 10 nA current. This was followed by fine milling using 500 pA current to polish the front view. Afterwards, imaging and milling (500 pA for a single slide conform 25 nm) at the front view were performed alternatively to obtain an image stack for the final tomography. The 3D model is reconstructed using the software "Octopus 8.6" and analysed using the image processing software "VGStudioMax2.2".

The focused ion beam was also used to slice fine lamellae from the cell wall of the foam to study the distribution of $MgAl_2O_4$ and MgO particles at the gas-solid interface using TEM. The sample preparation procedure is similar to that of FIB tomography described in the previous

paragraph. Milling steps with ion beam currents decreasing from 10 nA to,2 nA, to 200 pA were performed to extract the lamella. After extraction, the lamella was bonded to a copper grid and reduced to a thickness <100 nm using currents of 50 pA and 20 pA. The electron transparent lamella obtained was analysed using Zeiss LIBRA 200FE TEM operated at 200 kV accelerating voltage. An analytical TEM, Philips CM 30 was also used for imaging the $MgAl_2O_4$ particles in the lamella and to measure the elemental composition using EDX micro analysis.

3. Results

3.1 In-situ composite and the foam precursor

The X-ray diffraction spectrum of Al-11wt.%Si/$MgAl_2O_4$ in-situ composite is shown in Fig. 1(a). Peaks corresponding to $MgAl_2O_4$, Si, Al, eutectic phase of Mg_2Si peak and transition phases are clearly visible in the spectrum while the intensity of the MgO peak is small due to its low concentration. The SEM micrograph (Fig.1(b)) shows the pro-eutectic phases of the Al-11wt.%Si alloy and the agglomerated $MgAl_2O_4$ particles in the inter-dendritic region. At higher magnification (Fig.1(c)) the $MgAl_2O_4$ particles reveals their octahedral morphology. The EDX spot microanalysis spectrum taken from an octahedral phase confirms that those are $MgAl_2O_4$ particles (Fig.1(d)). MgO particles are even finer and cannot be identified in the microstructure.

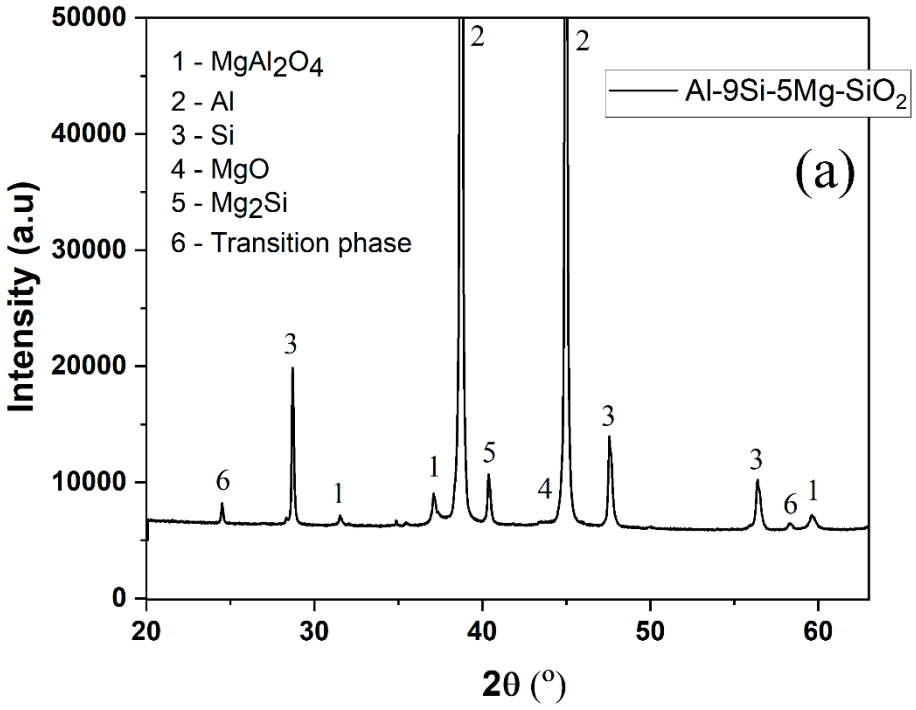

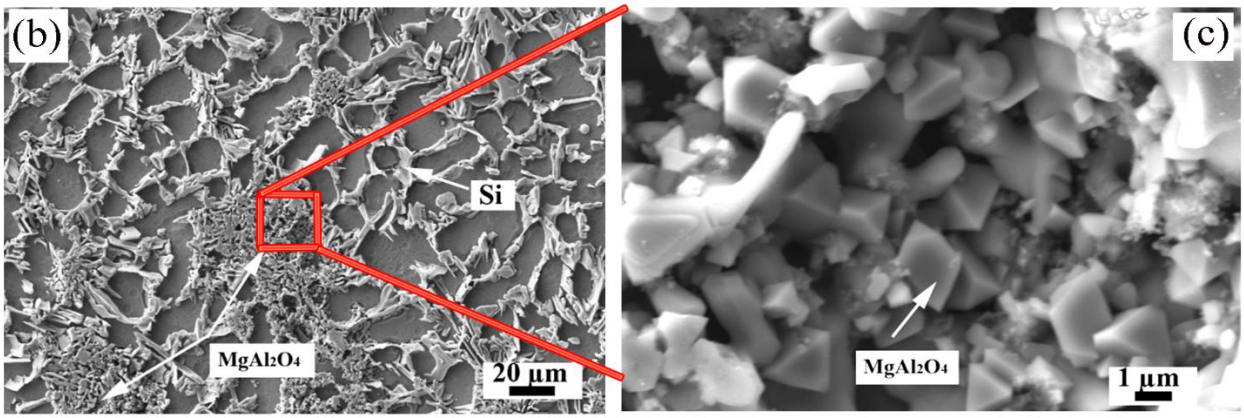

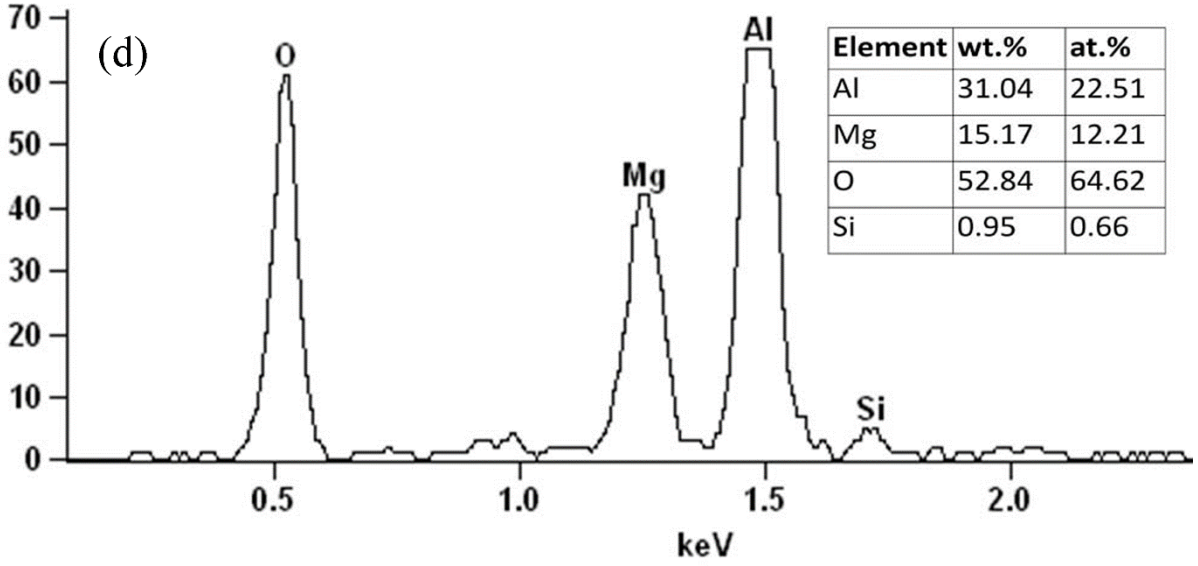

Element	wt.%	at.%
Al	31.04	22.51
Mg	15.17	12.21
O	52.84	64.62
Si	0.95	0.66

Fig.1 (a) XRD spectra of Al-11wt.%Si/$MgAl_2O_4$ in-situ composite showing the presence of $MgAl_2O_4$, Mg_2Si, MgO and transition phase (Mg-Al-O-Si) peaks along with the most intense peaks of Al and Si. (b),(c) SEM micrographs of the composite showing ultrafine $MgAl_2O_4$ (spinel) particles in the Al-11Si alloy matrix. (d) EDX micro analysis spectrum from the $MgAl_2O_4$ particle marked by a white arrow in Fig.1c, confirming the presence of Al, Mg, and O.

Figure 2 (a)-(c) shows optical micrographs of foamable Al-11Si/$MgAl_2O_4$ precursors containing various volume fractions of $MgAl_2O_4$ particles (3.4, 2.5 and 1.7 wt.%). The cross sections of all precursors exhibit pores of various sizes despite rapid solidification. The pore volume and the pore sizes in the rapidly solidified precursor is directly proportional to the concentration of the stabilizing particles. The precursor 3.4p exhibits a mixture of fine and large pores that are poorly distributed. The pores become smaller and more uniformly distributed in the precursors 2.5p and 1.7p as the particle concentration is reduced. The absolute density of the precursors containing 3.4p, 2.5p and 1.7p are 2.02, 2.29 and 2.4 g/cm^3, respectively (Table 2) implying decreasing porosity with decreasing particle content. Figure 2(d) and 2(e) show a SEM micrograph of the cross section of precursor 3.4p where the particles densely cover the gas-solid interface of the pores. At higher magnification (Fig.2(e)) the spinel particles in the gas-solid interface are clearly visible.

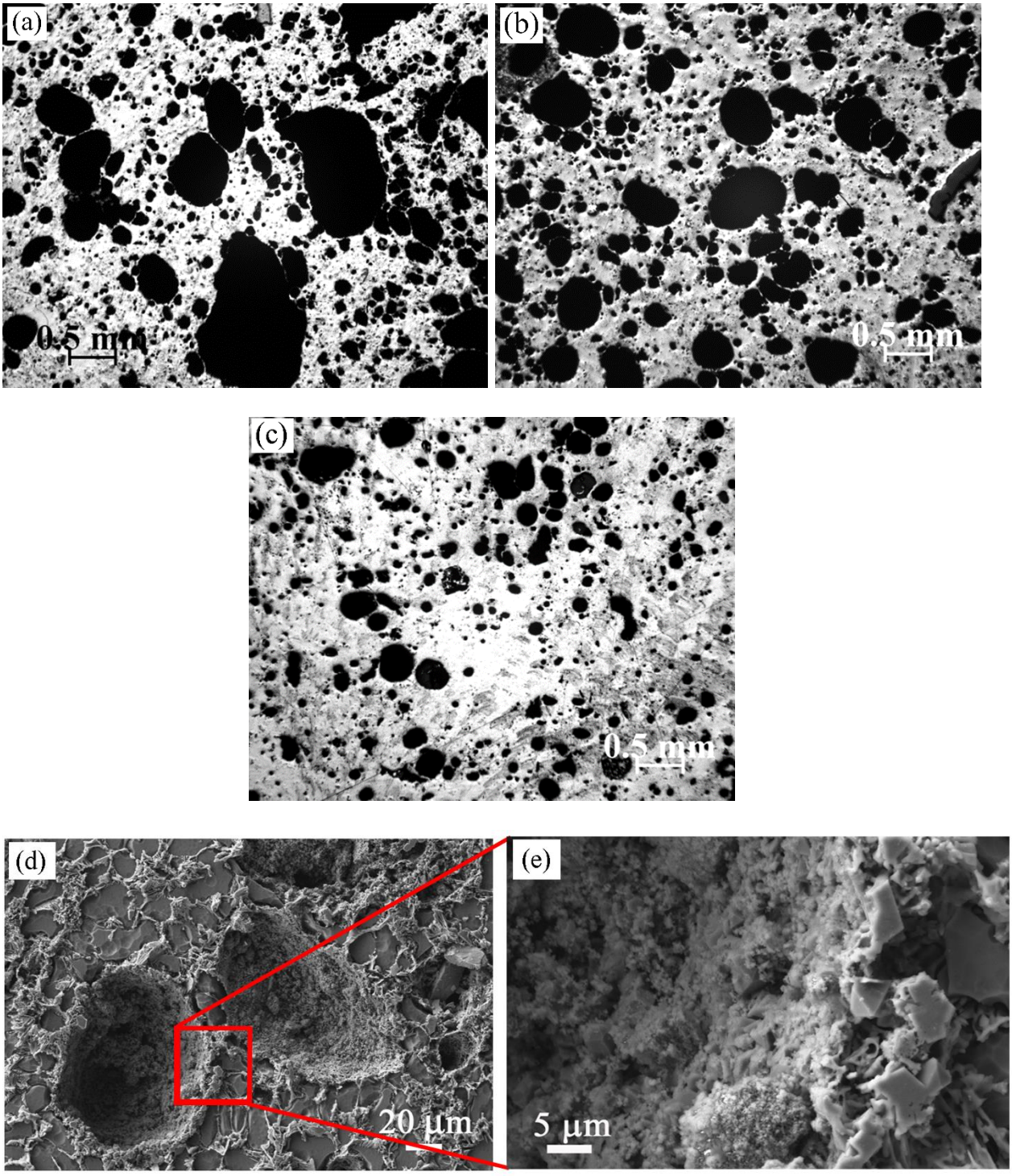

Fig.2 Optical micrograph of the cross section of foamable precursors of Al-11Si/$MgAl_2O_4$ (a) 3.4p (b) 2.5p and (c) 1.7p. (d) and (e) SEM micrograph of the cross-section of 3.4p precursor showing the pores and the presence of $MgAl_2O_4$ particles at the gas-solid interface.

3.2 In-situ analysis of foam evolution

Figure 3 (a)-(c) shows a sequence of X-ray radioscopic images taken from Al-11Si/$MgAl_2O_4$ foams (3.4p, 2.5p and 1.7p) during foaming after various interval (0 to 600 s). The sample at time zero is the cylindrical solid precursor which melts upon heating and expands for up to 600 s, after which the foam solidifies (last image). The foamable precursors exhibited fast approximately linear expansion once they had completely melted after 60 s followed by a decreasing expansion rate (Fig.3(d)). The 3.4p foam continously expands till the end of the foaming time (600 s) and exhibits the highes expansion (up to 470 %) than the 2.5p and 1.7p foams. Cell coalesence is prominent in the 2.5p and 1.7p foams during expansion. Accumulation of liquid at the bottom, also called '*gravity induced drainage'*, is observed in all the foams after 80 s and increasing with time especially in 1.7p foam. During solidification, only the 2.5p and 1.7p foams showed some shrinkage.

The macrostructures obtained by X-ray tomography of the solidified foams obtained after 600 s are shown at the end of each radioscopic image sequence. The tomographic cross section of 3.4p foam shows mostly uniform cell size distribution and thin cell walls, whereas the cross-sections of 2.5p and 1.7p foams feature non-uniform cell size distributions and a liquid sump at the bottom. The time-resolved density profiles as shown in Fig.4 demonstrate that drainage in the 2.5p and 1.7p foams is significantly different from that in 3.4p foam. For the 3.4p foam, there is hardly any change in the liquid fraction profile after full expansion, whereas in the other two foams, a significant build-up of a density step associated to drainage can be seen at the bottom of the foams after 300–400 s.

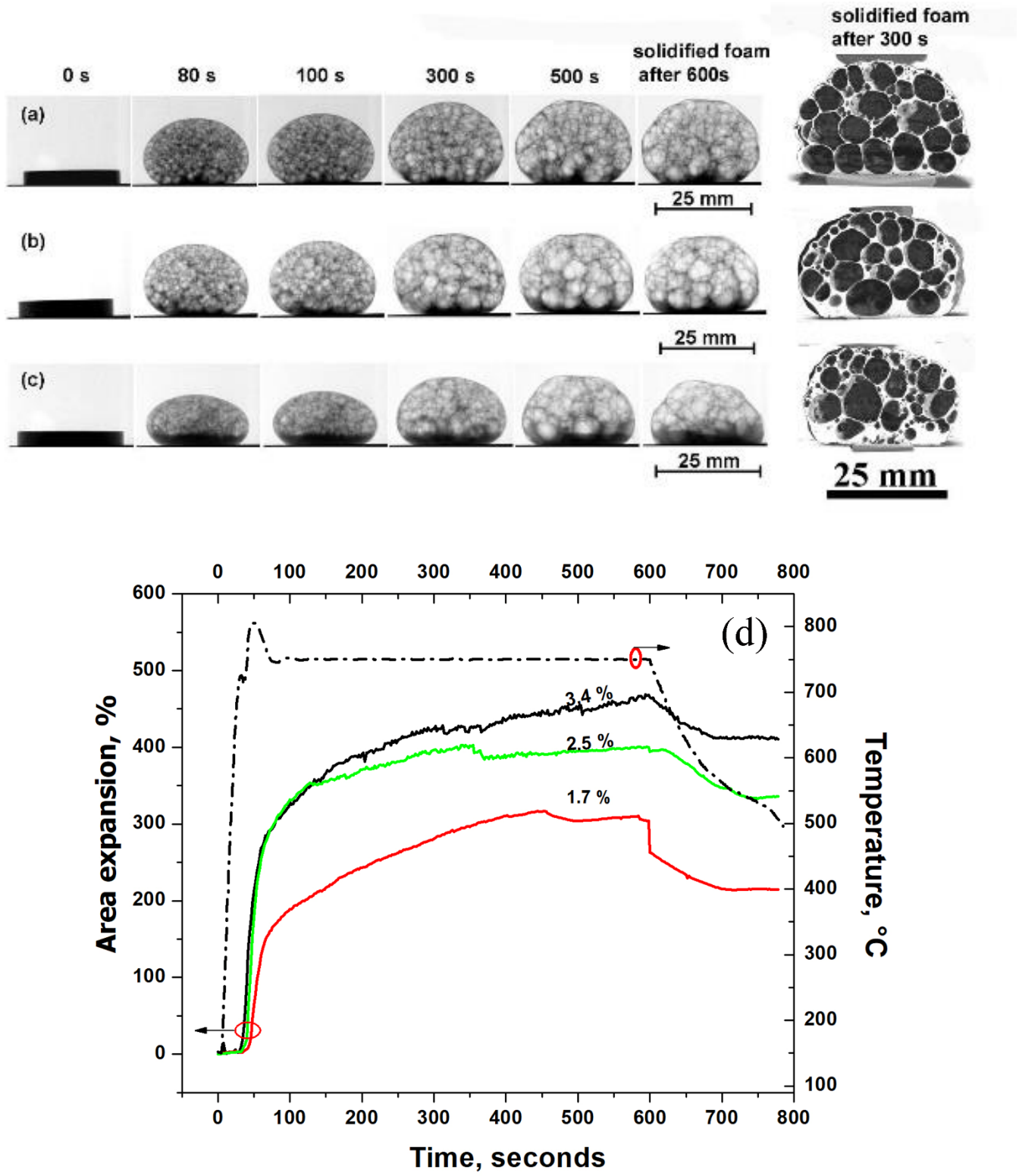

Fig.3 X-ray projection images of evolving foam (a) 3.4p, (b) 2.5p and (c) 1.7p baked at 750 °C for six different times. Solidified state is also represented by a tomographic 3D image. (d) Corresponding changes of foam projected area as a function of time. Upper curve (dotted line) is the sample temperature measured at the bottom of the foam.

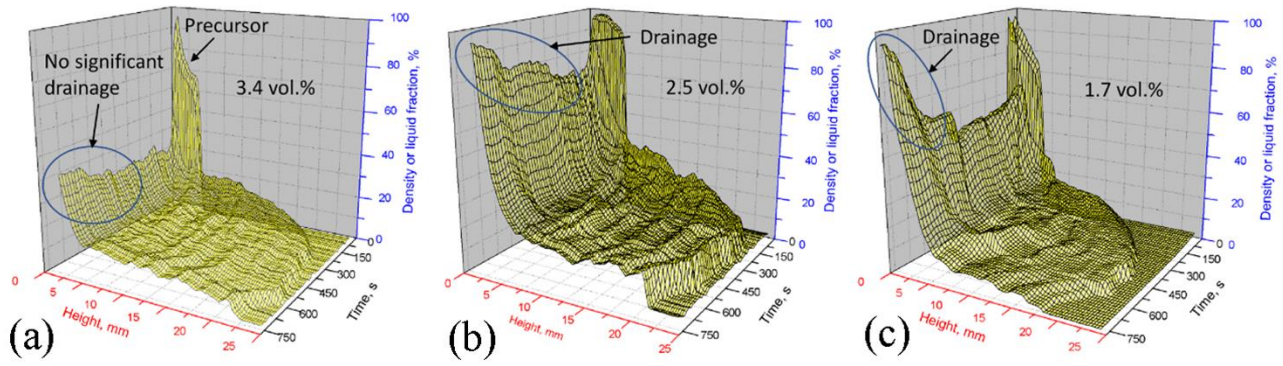

Fig.4 Time-resolved vertical density profiles in (a) 3.4p, (b) 2.5p and (c) 1.7p foams baked at 750 °C.

3.3 Microstructural characterization of foam cell wall

Figure 5(a),(b) show the SEM microstructure of a trench in the gas-solid interface of 3.4p foam cut by FIB to investigate the $MgAl_2O_4$ particle distribution in the cell wall closer to the gas-solid interface. The cell wall thickness of the 3.4p foams ranges from 100 µm to 200 µm. The wall chosen for FIB tomography was about 200 µm thick. The analysed volume is a 15 µm × 15 µm × 15 µm large cuboid from the trench which is composed of 300 slices with a thickness of each slice of 20 nm. The SEM micrograph (Fig.5(c)) of a FIB slice shows $MgAl_2O_4$ particles embedded in the gas solid interface. Inside the cell wall, large plates of eutectic Si are visible. Figure 5(d) shows the 3D rendering of the $MgAl_2O_4$ particles in the gas solid interface. A closer view shows clearly the octahedral morphology of $MgAl_2O_4$ particles (Fig.5(e)). In addition, Figure 5(e) shows finer non-faceted particles embedded in the gas solid interface. MgO particles may be present at the gas solid interface, however, it was difficult to detect them in SEM.

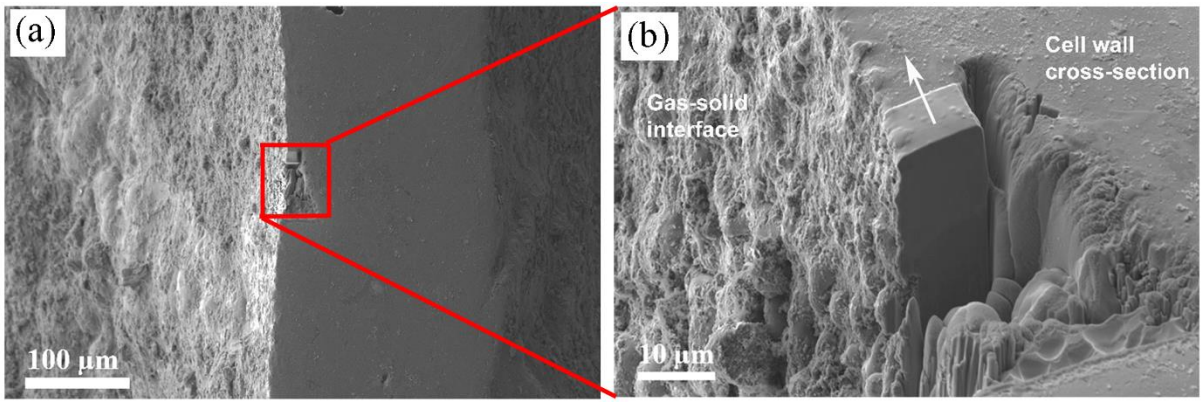
(a)
100 μm
(b)
Gas-solid interface
Cell wall cross-section
10 μm

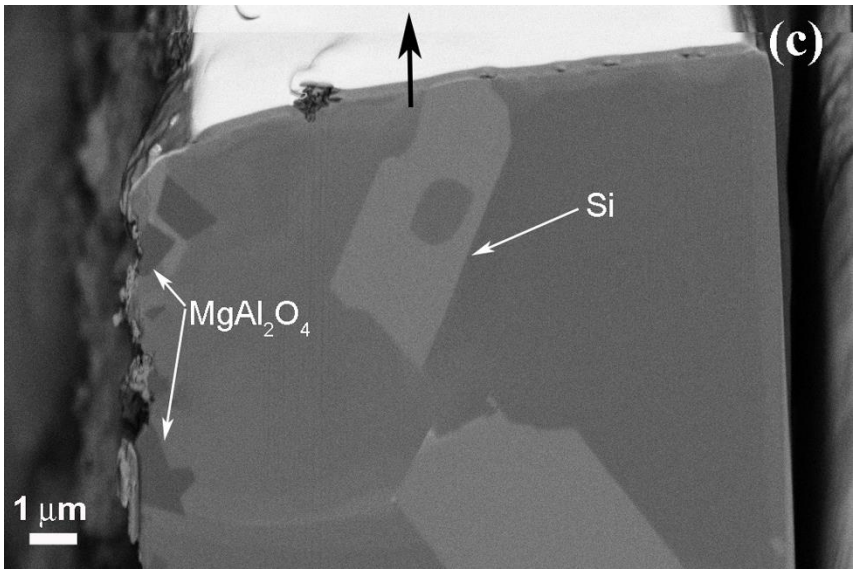
(c)
Si
MgAl2O4
1 μm

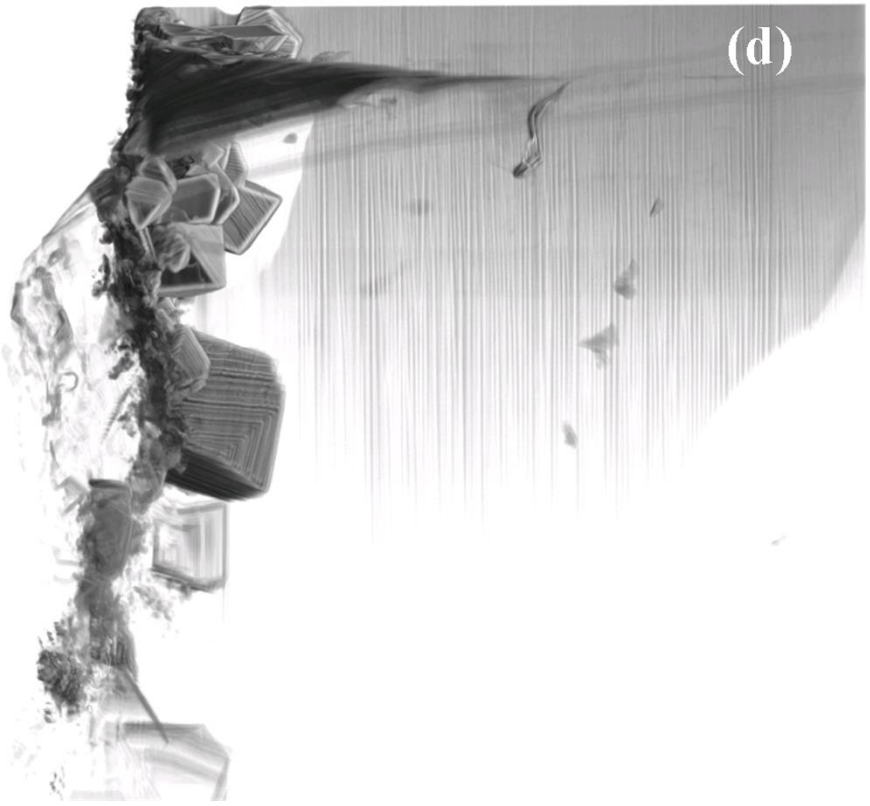
(d)

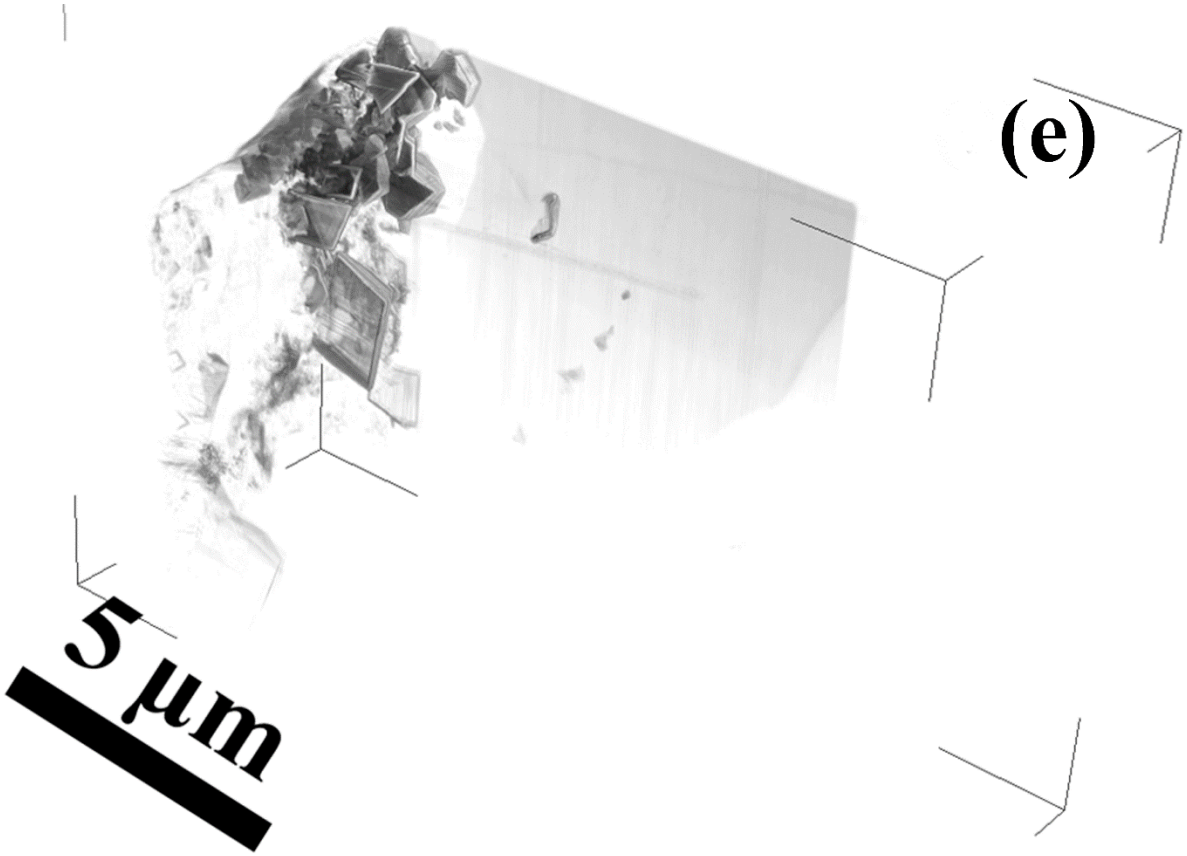

Fig.5 SEM micrograph of a cell wall cross-section of 3.4p foam. (a) View of the cell-wall cross section including a trench cut into the gas-solid interface by FIB. (b) Side view of trench showing the area of FIB slicing. Arrow indicates the direction of FIB slicing. (c) SEM micrograph of a FIB slice of thickness 20 nm. (d) 3D rendering of $MgAl_2O_4$ particles in the gas-solid interface of the trench (front view). (e) 3D rendering of $MgAl_2O_4$ particles and the surface oxides in the gas solid interface (side view)

The gas-solid interface was further investigated by TEM. A sample was prepared by slicing a lamella in the foam cell wall using FIB. The gaseous side of the interface was platinum coated to protect the oxide layer. Figure 6(a) shows a bright field image of a cell wall cross-section closer to the gas-solid interface of the 3.4p foam. A thick oxide layer is visible in the gas-solid interface into which the octahedral shaped $MgAl_2O_4$ particles are embedded. The $MgAl_2O_4$ particles observed in the lamella are less than 100 nm big. The selected area diffraction pattern

associated to the bright field image is shown in Fig.6(b). From the position of the diffraction rings a number of d-spacing and hkl planes derived from the diffraction pattern indicates $MgAl_2O_4$ of FCC crystal structure. Figure 6 (c),(d) show a bright-field image of the gas-solid interface of the foam cell wall and the corresponding EDX analysis. We can clearly see two different types of particles: The first ones are faceted and embedded in the oxide layer of the gas-solid interface and the second ones are ultra-fine particles present on the oxide layer. The EDX spot microanalysis spectra and corresponding compositional measurement confirm that those particles are $MgAl_2O_4$ and MgO, respectively. The silicon signal comes from the alloy matrix.

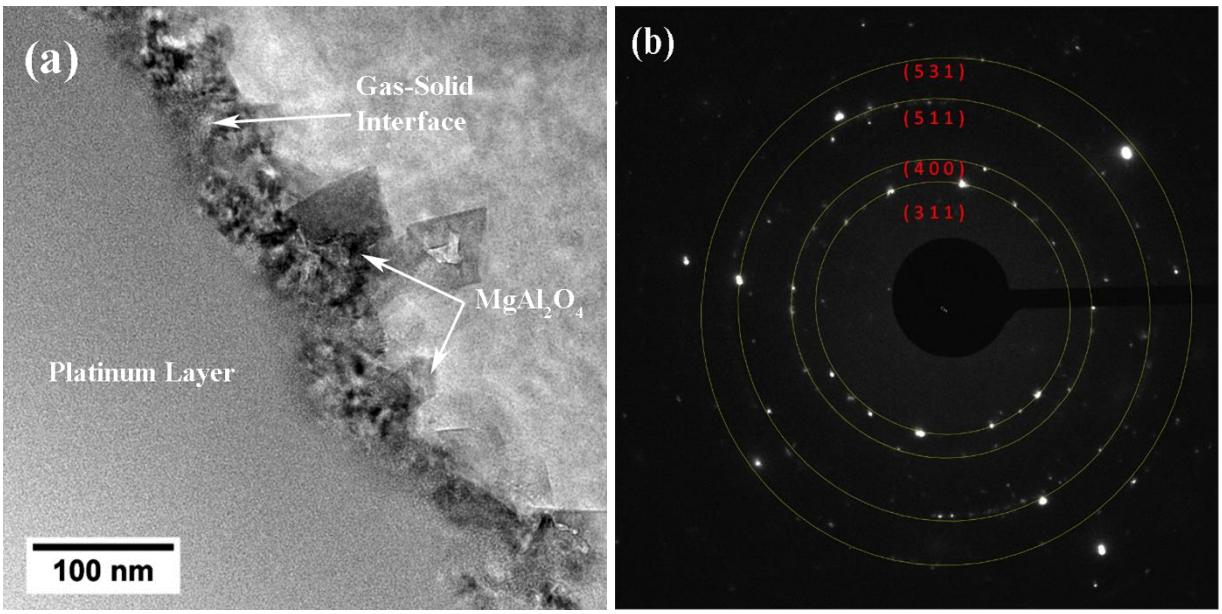

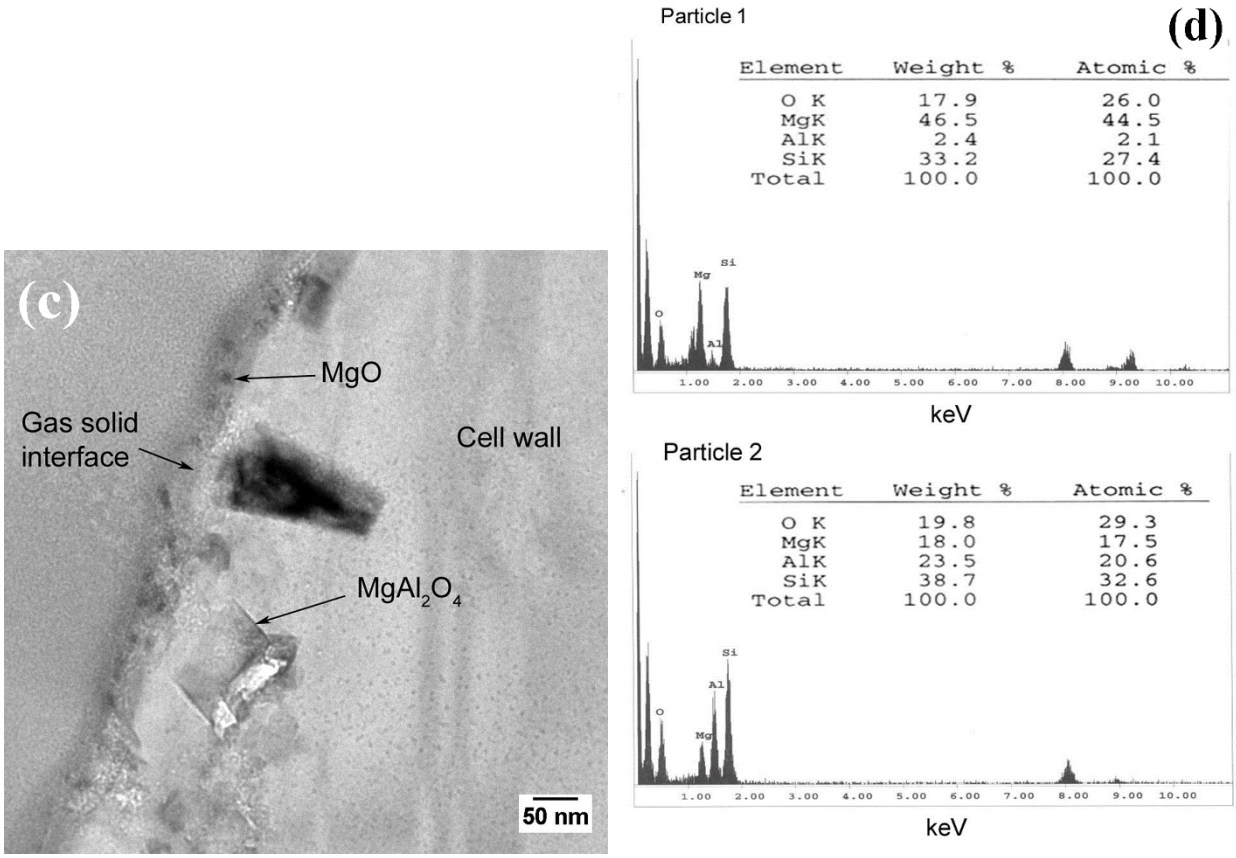

Fig.6 (a) Bright-field TEM image showing $MgAl_2O_4$ particles at the gas-solid interface of 3.4p foam. (b) Selected area diffraction (SAD) pattern of $MgAl_2O_4$ particle. (c) Bright field image showing MgO and $MgAl_2O_4$ particles in the gas solid interface. (d) The EDX spot micro analysis, spectra of particle 1 (MgO) and particle 2 ($MgAl_2O_4$).

4. Discussion

$MgAl_2O_4$ (spinel) occurs as a fine octahedrally shaped particle formed via the reaction of Mg and SiO_2 in molten Al, as explained in Ref. [29,30]. A complete reaction to $MgAl_2O_4$ alone in the matrix depends on time, temperature, concentration of Mg and SiO_2 particles and the size and morphology of SiO_2 [14,30]. In the present study, micro-silica particles of 44 μm size were used to enhance the reaction since micro-silica particles are porous, which favours a more complete reaction. A reaction temperature of 750 °C and a long reaction time of 10 h were chosen to ensure predominant $MgAl_2O_4$ formation and to minimise MgO formation. Although

in the initial reaction stage, MgO forms as the dominant phase due to the high Mg concertation (5 wt.%), allowing the reaction to continue for a longer time converts MgO into $MgAl_2O_4$ through various transition phases such as Mg-Al-O-Si and Mg-Al-O [30].

During precursor fabrication, the rapid solidification of the foamable melt is intended to prevent the TiH_2 from decomposing. However, due to the time between TiH_2 addition and pouring the melt into the water-cooled copper mould, some TiH_2 powder particles do start to decompose and release some hydrogen gas causing the formation of fine pores in the precursor. The porosity eventually present in the precursor is the highest for the highest $MgAl_2O_4$ concentration (see density values in Table 2). A high particle concentration facilitates gas nucleation at those particles during the mixing of TiH_2 and solidification.

During solidification of aluminium melt, when the local hydrogen concentration exceeds the solubility limit (super-saturation) at a particular temperature, at the liquid-solid interface pore forms and grows with no surface energy barrier required to overcome (nucleation). Such hydrogen super-saturation will increase with an increase in the solidification rate. Pores can also form away from the liquid-solid interface where it has low super-saturation of hydrogen or the low pressure inside the pore indicating no surface energy barrier to overcome. [31]. Thomas & Gruzleski analysed the literature data on the hydrogen concertation in the melt required for the pore formation in aluminium castings. From the analysis a threshold hydrogen level (approximately 0.1 to 0.2 mL/100g.Al), was estimated, which is found to be above the hydrogen solubility in solid Al and its alloys. Below this threshold hydrogen level, no pore formation is possible in the castings. [32] Chen & Gruzleski have shown that the poor melt quality such as the presence of oxides and spinels in the Al melt decreases the threshold hydrogen level in relation to the pore formation and increases the sensitivity of amount of pore

formation to the hydrogen concentration. [33] However, the mechanism behind how these inclusions contributes to the pore formation in the solid castings is unclear, except the bi-film theory proposed by Campbell [34].

In the literature it has been shown that oxides can act as heterogeneous nucleating sites for pores due to their partial wettability with aluminium [7,35-38]. In our study it is clearly seen that the initial decomposition of TiH_2 in the composite melt aids in the pore formation in the precursor castings. However, a clear difference in the pore volume of the precursors with respect to the particle concentration confirms the nucleation of pores by the particles. Microstructurally, the coverage of the pore surfaces by the $MgAl_2O_4$ particles in the 3.4p precursor also confirms the role of the particles on pore nucleation. The decrease in $MgAl_2O_4$ concentration decreases the pore nucleation as it is evident from the 2.5p and 1.7p precursors. During re-melting of the precursors, the entrapped gas in the pores expand and contributes to foaming. However, a major part of the bubbles is created due to continuous decomposition of TiH_2 and nucleation of the released hydrogen with the help of the of $MgAl_2O_4$ particles as nucleating sites.

The expansion, stabilization and drainage in the foams as a function of time varies with respect to the $MgAl_2O_4$ particles concentration. Vinod Kumar et al. have shown that 3.4 vol.% of fine (80 nm to 1 μm size) octahedrally shaped $MgAl_2O_4$ particles effectively stabilize the Al foams that were foamed for 100 s or 150 s [14]. Decreasing the concentration of $MgAl_2O_4$ to 2.5 or 1.7 vol.% leads to a decrease in expansion for both 100 s or 150 s of foaming time, but still a good pore structure is obtained [39]. The present work supports these previous observations and in addition the in-situ foam evolution and drainage studies gives an understanding on the stabilization behaviour of the aluminium foams with $MgAl_2O_4$ particles.

In-situ X-ray radioscopy investigation of foam evolution shows that 3.4p foam is highly stable, features good expansion, minimum drainage and coalescence for 600 s of isothermal holding. The 2.5p and 1.7p foams, in contrast, show significant drainage, which has an adverse effect on foam expansion and pore structure when held for 600 s. The stable foaming with relatively larger expansion and minimum drainage observed in 3.4p foam can be correlated to the enhanced melt viscosity caused by the fine $MgAl_2O_4$ particles dispersed in large numbers [2,9,19]. $MgAl_2O_4$ particles in the melt also restricts gravity-driven melt flow along cell walls and Plateau borders, which can also be seen as an increased apparent viscosity [40]. $MgAl_2O_4$ particles are found to attached to the gas-solid interfaces of the foam which could reduce the capillary-driven drainage by modification of cell wall curvatures [14]. All this results in a reduced rate of liquid drainage and thus a more stable foam [1,2,5].

Decreasing the concentration of $MgAl_2O_4$ particles from 3.4 vol.% to 1.7 vol.% in the composite melt may not significantly decrease its actual viscosity. But the structure of the cell wall in the foam gets modified due to a reduced number of particles attached to the gas solid interface and an increase in the number of mobile particles, which decreases the effective viscosity of the melt and causes drainage. On the other hand, lower concentrations of $MgAl_2O_4$ particles also imply a reduced number density in the cell wall, i.e., easier melt flow in the films. Similarly, there could be a decrease in the surface tension with the decrease in the $MgAl_2O_4$ particles concentration in composite melt, however, it has a negligible effect in foam stabilization in comparison to viscosity [41].

The FIB tomograms show that octahedrally shaped $MgAl_2O_4$ particles of different sizes ranging from nm-sized to µm-sized are densely packed and tightly bound in a thick oxide skin at the gas solid interface of 3.4p foam cell wall (Fig. 5d&e). The analysed volume is small (15

μm × 15 μm × 15 μm) in comparison to the cell wall thickness of ~200 μm and no $MgAl_2O_4$ particles were found at the top or at the centre of the analysed film. Similar way the TEM analysis of the gas-solid interface reveals that $MgAl_2O_4$ particles of <100 nm size are tightly bound together and embedded in the oxide skin and finer MgO particles are found inside the oxide skin of thickness ~50 nm (Fig.6(c)) and no particles are found away from the gas-solid interface. However, particles may be present in the region discretely from the gas-solid interface, which may not have covered under the analysed area in both FIB tomography and TEM.

The wettability of the particles with liquid aluminium is essential for the stabilization of foam. Particles which have a contact angle less <90 ^{o} stabilize the foam and >90 ^{o} destabilize it. In particular, the particles which have a contact angle of 70–86^o have partial wetting characteristic and can effectively stabilize the foam by attaching themselves to the gas solid interface of a cell wall [2, 3, 15,16]. Kaptay's particle arrangement model shows that in addition to the particles that attached to the gas solid interface, particles also connect the two opposite interfaces of a liquid metal film by forming a bridge to produce a mechanical disjoining forces for stabilization [5]. In the microstructures of solid aluminium foams stabilized by various particles such as SiC, Al_2O_3, TiB_2 or ZrB_2, particles are found to be attached to the gas solid interface, and also inside the cell lamella the particles are appearing to be engulfed in the grain boundaries of Al since the particles are pushed by the growing Al grain during solidification [2,6,11,12,18]. Therefore, even though a particle bridge was formed in the liquid film, it cannot be retained in the solid foam due to solidification effect [18]. Haibel et al. have shown in their X-ray tomographic analysis of solid Al foam stabilized by SiC that the particle density measured is larger at the gas solid interface in comparison to the particle density at the centre

of the cell lamella and therefore it is unlikely to assume that a liquid film had a bridge connecting opposite interfaces [18].

The $MgAl_2O_4$ possesses FCC crystal structure and has small lattice misfit (1.4%) with pure Al, and therefore proven to be an effective nucleating site for α-Al. However, this lattice misfit may vary for aluminium containing solute elements [42]. Because of these characteristics, $MgAl_2O_4$ particles are not pushed to the grain boundaries by the growing Al grains during solidification [43] and therefore their arrangement in the liquid foam is retained in the solid foam. This is evident from the two different microstructures of the gas solid interfaces of aluminium foam stabilized by $MgAl_2O_4$ [14] and TiB_2 particles *(unpublished result)* shown in Fig.7(a) and 7(b). The $MgAl_2O_4$ particles show uniform distribution (Fig.7(a)) whereas the TiB_2 particles are found to be agglomerated in the grain boundaries of Al grain. (Fig.7(b)). Both, $MgAl_2O_4$ and TiB_2, particles in these cases are submicron sized particles and their concentration in the aluminium foam is similar, 3.4 vol.% and 3 vol.%, respectively.

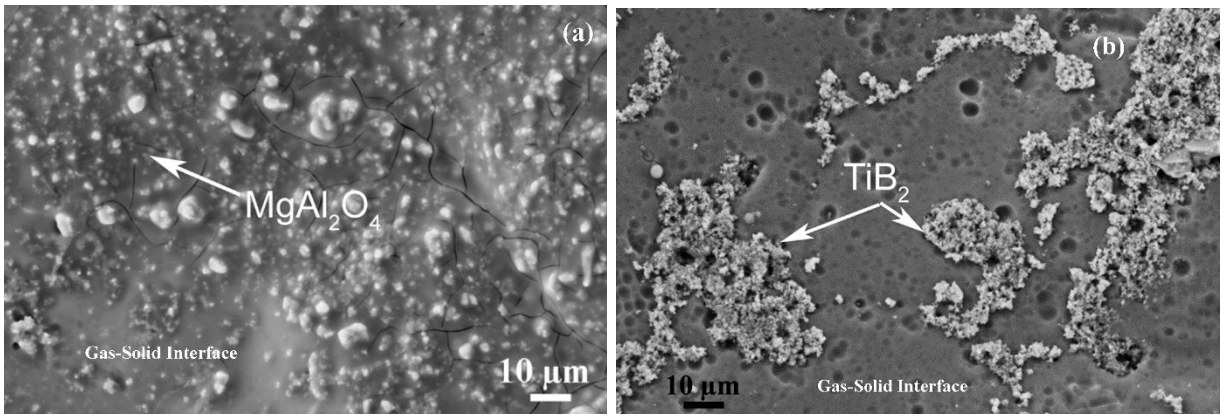

Fig.7 SEM micrographs of gas-solid interface of aluminium foam stabilized by (a) $MgAl_2O_4$ particles and (b) TiB_2 particles.

$MgAl_2O_4$ particles do not form a bridge in the liquid film. Instead, they are tightly bound to the gas-liquid interface of the liquid film for stabilization. This is supported by the earlier proposed

mechanism of Haibel et al. that the liquid metal foam is stabilized only by the interaction between the particles attached to one side of the film thereby creating a surface elasticity that prevents the rupture of the liquid film. They further observed that the particles do not form bridges across the interface to produce a mechanical disjoining pressure [18]. It was also suggested that the interaction can be improved by employing nano-sized particles at lower vol.% for stabilization [18]. The nano-sized $MgAl_2O_4$ particles closely embedded to the oxide skin of the gas-solid interface seen in Fig. 6(a) approves the above suggestion. The 1.7p foam would have exhibited high stability, if the precursor had larger number of nano-sized $MgAl_2O_4$ particles in the precursor, however, it is not possible to process nano-sized $MgAl_2O_4$ particles in Al composite via in-situ method.

The attachment of $MgAl_2O_4$ particles at the gas-solid interface is attributed to the thick oxide skin as observed in Fig.6(a) and 6(c). Studies on individual films have shown that an oxide layer is essential to obtain a stable film as it immobilises the stabilizing particles. The studies have also shown that a certain amount of oxygen is important for foaming and how that oxygen is get converted into oxide skin and immobilizes the particles [21].

5. Summary

- The way $MgAl_2O_4$ particles stabilise emerging liquid Al-Si alloy foam was studied via in-situ X-ray radioscopic technique and FIB tomographic visualization of the gas-solid interface of the solidified foam.
- An “interrupted foaming technique” was applied. It was found that the stabilizing particles also act as nucleating sites for gas bubbles and a higher concentration of particles increases the bubble nucleation rate.

- Ultrafine $MgAl_2O_4$ (spinel) particles effectively stabilise Al-11wt.%Si alloy foam at a concentration of 3.4 vol.%. Decreasing the particle concentration causes drainage and affects the expansion of the foam. The in-situ X-ray radioscopic measurements allowed us to calculate the expansion and drainage of the liquid foams as a function of time and particle concentration.
- FIB tomography and TEM analyses show that the $MgAl_2O_4$ particles are densely embedded in the oxide skin of the gas-solid interface of a cell wall. Particles embedded in the gas-solid interface slow down liquid flow in the films, and thus reduce drainage. No particles were found away from the gas-solid interface in the analysed volume of the cell wall.
- Stabilization of foam is due to the $MgAl_2O_4$ particles interaction at the gas solid interface of a liquid film. Particles interaction across the interface in the form of bridge is not essential for foam stabilization.

Acknowledgement: This study was supported by the German Research Foundation (DFG), grants GA 1304/2-1

Conflict of Interest: On behalf of all authors, the corresponding author states that there is no conflict of interest

Reference

[1] J. Banhart, Metal Foams: Production and Stability, Adv. Eng. Mater. 8 (2006) 781-794, https://doi.org/10.1002/adem.200600071

[2] S.W. Ip, Y. Wang, J.M. Toguri Aluminum foam stabilization by solid particles. Can. Metall. Q 38 (1999) 81–92. https://doi.org/10.1016/S0008-4433(98)00024-X.

[3] C. Körner, M. Arnold, R.F. Singer, Metal foam stabilization by oxide network particles. Mater. Sci. Eng. A 396 (2005) 28–40. https://doi.org/10.1016/j.msea.2005.01.001

[4] C. Körner, Foam formation mechanisms in particle suspensions applied to metal foams. Mater. Sci. Eng. A 495 (2008) 227–235. https://doi.org/10.1016/j.msea.2007.09.089

[5] G. Kaptay, Interfacial criteria for stabilization of liquid foams by solid particles, Colloids Surfaces A: Physicochem. Eng. Asp. 230 (2004) 67–80. https://doi.org/10.1016/j.colsurfa.2003.09.016.

[6] N. Babcsán, D. Leitlmeier, H.P. Degischer, Foamability of particle reinforced aluminum melt. Materwiss Werksttech 34 (2003) 22–29. https://doi.org/10.1002/mawe.200390011.

[7] G. S. Vinod Kumar, M. Mukherjee, F. Garcia-Moreno, J. Banhart, Reduced Pressure foaming of aluminium alloys, Metall. Mater. Trans. A 44 (2003) 419–426. https://doi.org/10.1007/s11661-012-1398-8

[8] G. S. Vinod Kumar, F Garcia Moreno, J.Banhart, A. R. Kennedy, The stabilizing effect of oxides in foamed aluminium alloy scrap, Int. J. Mater. Res 106 (2015) 978-987. https://doi.org/10.3139/146.111255

[9] K. Heim, F. García-Moreno, J. Banhart, Particle size and fraction required to stabilise aluminium alloy foams created by gas injection, Scr. Mater. 153 (2018) 54–58. https://doi.org/10.1016/j.scriptamat.2018.04.041

[10] N. V. Ravi Kumar, N. Ramachandra Rao, B. Sudhakar, A.A. Gokhale, Foaming experiments on LM25 alloy reinforced with SiC particulates, Mater. Sci. Eng. A 527 (2010) 6082–6090. https://doi.org/10.1016/j.msea.2010.06.024

[11] N Babscan G. S. Vinod Kumar, B. S. Murty, J. Banhart, Grain refiners as liquid metal foam stabilizers, Trans. Indian Inst. Met 60 (2007) 127-132

[12] S. Sasikumar, K. Georgy, M. Mukherjee, G. S. Vinod Kumar, Production, stability and Mechancial properties of in-situ Al-ZrB_2 particle stabilized foams, Mater. Sci. Eng. A 849 (2022) 143501. https://doi.org/10.1016/j.msea.2022.143501

[13] Y. H. Song, T. Masakazu, I. Takuya S. Yoshihiro, B-Y Hur, H-Nakajima, Fabrication of Al-3.5Pct Si-0.18 Pct Mg Foam Strengthened by AlN Particle Dispersion and its Compressive Properties, Metall. Mater. Trans. A 41 (2010) 2104–2111.

https://doi.org/10.1007/s11661-010-0247-x

[14] G. S. VinodKumar, M. Chakraborty, F. Garcia-Moreno, J. Banhart, Foamability of $MgAl_2O_4$ (spinel) – reinforced aluminium alloy composites, Metall. Mater. Trans. A 42 (2011) 2898-2908. https://doi.org/10.1007/s11661-011-0709-9

[15] Y.Q. Sun, T. Gao, The optimum wetting angle for the stabilization of liquid-metal foams by ceramic particles: Experimental simulations, Metall. Mater. Trans. A 33 (2002) 3285–3292. https://doi.org/10.1007/s11661-002-0315-y.

[16] G. Kaptay, Interfacial criteria for ceramic particle stabilised metallic foams, in: J. Banhart, M.F. Ashby, and N.A. Fleck (Eds.), Metal Foams and Porous Metal Structures, MIT Verlag, Bremen, Germany. 1999, pp. 141-45.

[17] H. Kumugai, Y. Torikata, H. Yoshimura, M. Kato, T. Yano, Estimation of the stability of foam containing hydrophobic particles. Agric. Biol. Chem. 55 (1991) 1823-1828. https://doi.org/10.1080/00021369.1991.10870871

[18] A. Haibel, A. Rack, J. Banhart, Why are metal foams stable?, Appl. Phys. Lett. 89 (2006) 3–6. https://doi.org/10.1063/1.2357931

[19] S. Bhogi, J. Nampoothiri, K.R. Ravi, M. Mukherjee, Influence of nano and micro particles on the expansion and mechanical properties of aluminum foams, Mater.Sci. Eng. A 685 (2017) 131–138. https://doi.org/10.1016/j.msea.2016.12.127

[20] K. Heim, G. S. Vinod Kumar, F. Garcia-Moreno, I Manke, J. Banhart, Drainage of particles stabilized aluminium composites through single films and plateau borders, Colloids and Surfaces A: Physicochem. Eng. Asp. 438 (2013) 85-92. https://doi.org/10.1016/j.colsurfa.2013.02.019

[21] K. Heim, G. S. Vinod Kumar, F. Garcia-Moreno, A. Rack, J. Banhart, Stabilization of aluminium foams and films by the joint action of dispersed particles and oxide films, Acta Mater. 99 (2015) 313-324. https://doi.org/10.1016/j.actamat.2015.07.064

[22] G. S. Vinod Kumar, K. Heim, J. Jerry, F. Garcia-Moreno, A. R. Kennedy, J. Banhart, Effect of magnesium addition on the cell structure of foams produced from re-melted aluminium alloy scrap Metal. Mater. Trans. B 48 (2017) 2551–2563. https://doi.org/10.1007/s11663-017-1043-4

[23] S. Bhogi, M. Mukherjee, Foam stabilization by Magnesium, Mater. Lett. 200 (2017) 118-120. https://doi.org/10.1016/j.matlet.2017.04.100

[24] Z Feng, Z Wei, X Su, Q Gao, G Xu, P Huang, W Wang, Foamability and mechanical properties of in situ submicron $MgAl_2O_4$p/Al composite foams by ultrasonic method, Mater. Lett. 326 (2022) 132968 https://doi.org/10.1016/j.matlet.2022.132968

[25] K. Heim, G. S. Vinod Kumar, F. Garcia-Moreno, J. Banhart, Stability of various particle-stabilized aluminium alloy foams made by gas-injection, J Mater. Sci. 52 (2017) 6401-6414. https://doi.org/10.1007/s10853-017-0874-3

[26] V. Gergely, B. Clyne, The FORMGRIP Process: Foaming of reinforced metal by gas release in precursor, Adv. Eng. Mater. 2 (2000) 175-178. https://doi.org/10.1002/(SICI)1527-2648(200004)2:4<175::AID-ADEM175>3.0.CO;2-W

[27] F. Garcia-Moreno, N. Babscan, J. Banhart, X-ray radioscopy of liquid metal foam: influence of heating profile, atmosphere and pressure, Colloids Surfaces A Physicochem Eng. Asp. 263 (2005) 290-294. https://doi.org/10.1016/j.colsurfa.2004.12.044

[28] F. Garcia-Moreno, M. Fromme, J. Banhart, Real-time X-ray radioscopy on Metallic foams using a compact micro-focus source, Adv. Eng. Mater. 6 (2004) 416-420. https://doi.org/10.1002/adem.200405143

[29] V.M. Sreekumar, K. R. Ravi, R. M. Pillai, B.C. Pai, M. Chakraborty, Thermodynamics and kinetics of the formation of Al_2O_3/$MgAl_2O_4$/ MgO in Al–silica metal matrix

composite, Metall. Mater. Trans. A 39 (2008) 919–933. https://doi.org/10.1007/s11661-007-9448-3

[30] V.M. Sreekumar, R. M. Pillai, B. C. Pai, M. Chakraborty, Evolution of $MgAl_2O_4$ crystals in Al-Mg-SiO_2 composites, Appl. Phy. A 90 (2008) 745-752. https://doi.org/10.1007/s00339-007-4357-2

[31] T. Murat (2020) The Effect of Hydrogen on Pore Formation in Aluminium Alloy Castings: Myths Versus Reality. Metals 368: 1-17. https://doi.org/10.3390/met10030368

[32] P.M. Thomas, J.E. Gruzleski, Threshold hydrogen for pore formation during the solidification of aluminium alloys, Metall. Trans. B 9 (1978) 139–141. https://doi.org/10.1007/BF02822681

[33] X.-G. Chen, J.E. Gruzleski, Influence of melt cleanliness on pore formation in aluminium—silicon alloys, Int. J Cast. Met. Res. 9 (1996) 17–26. https://doi.org/10.1080/13640461.1996.11819640

[34] J. Campbell, Complete Casting Handbook: Metal Casting Processes, Metallurgy, Techniques and Design, first ed, Elsevier Science, Amsterdam, 2011.

[35] S.N. Sahu, A.A. Gohale, A. Mehra, Prediction of Bubble Size Distribution in Aluminium Foam as a Function of %Titanium Hydride Addition, Trans. Indian Inst. Met. 70 (2017) 1981–1994. https://doi.org/10.1007/s12666-016-1020-7

[36] S.N. Sahu, A.A. Gohale, A. Mehra, Modelling nucleation and growth of bubbles during foaming of molten aluminium with high initial gas super-saturation, J. Mater. Proc. Tech. 214 (2014) 1-12. https://doi.org/10.1016/j.jmatprotec.2013.07.009

[37] S. N. Tiwari and J. Beech, The origin of gas bubbles in aluminium. Met. Sci. 12 (1978) 356-362. https://doi.org/10.1179/msc.1978.12.8.356

[38] C.C. Yang, H. Nakae, The effects of viscosity and cooling conditions on the foamability of aluminium alloy, J Mater. Proc. Tech. 141 (2003) 202–206. https://doi.org/10.1016/S0924-0136(02)01048-8

[39] J. Banhart, G. S. Vinod-Kumar, P.H. Kamm, T. R. Neu, F. Garcia-Moreno, Light-metal foams: Some recent developments, Ciencia and Tecnologia dos Materiais 28 (2016) 1-4. https://doi.org/10.1016/j.ctmat.2016.06.002

[40] V. Gergely, T.W. Clyne, Drainage in standing liquid metal foams: Modelling and experimental observations, Acta Mater. 52 (2004) 3047–3058. https://doi.org/10.1016/j.actamat.2004.03.007.

[41] F. Garcia-Moreno, S.T. Tobin, M. Mukherjee, C. Jimenez, E. Solorzano, G. S. Vinod Kumar, S. Hutzler, J. Banhart, Analysis of liquid metal foams through X-ray radioscopy and microgravity experiments, Soft Mater 10 (2014) 6955-6962. https://doi.org/10.039/c4sm00467a

[42] H.-T. Li, Y. Wang, Z Fan, Mechanism of enhanced heterogeneous nucleation during solidification in binary Al-Mg alloys, Acta Mater. 60 (2012) 1528-1537. https://doi.org/10.1016/j.actamat.2011.11.044

[43] P. S. Mohanty, J. E. Gruzleski, Mechanism of grain refinement in aluminium, Acta Metall. Mater. 43 (1995) 2001-2012. https://doi.org/10.1016/0956-7151(94)00405-7